

HyperFusion: A Hypernetwork Approach to Multimodal Integration of Tabular and Medical Imaging Data for Predictive Modeling

Daniel Duenias^a, Brennan Nichyporuk^{b,c}, Tal Arbel^{b,c}, Tammy Riklin Raviv^a, ADNI*

^aBen Gurion University of the Negev, blvd 1, Beer Sheva 84105, Israel

^bCentre for Intelligent Machines, McGill University, 3480 University St, Montreal, QC, H3A 0E9, Canada

^cMila - Quebec AI Institute, 6666 Rue Saint-Urbain, Montréal, QC H2S 3H1, Canada

Abstract

The integration of diverse clinical modalities such as medical imaging and the tabular data obtained by the patients' Electronic Health Records (EHRs) is a crucial aspect of modern healthcare. The integrative analysis of multiple sources can provide a comprehensive understanding of a patient's condition and can enhance diagnoses and treatment decisions. Deep Neural Networks (DNNs) consistently showcase outstanding performance in a wide range of multimodal tasks in the medical domain. However, the complex endeavor of effectively merging medical imaging with clinical, demographic and genetic information represented as numerical tabular data remains a highly active and ongoing research pursuit.

We present a novel framework based on hypernetworks to fuse clinical imaging and tabular data by conditioning the image processing on the EHR's values and measurements. This approach aims to leverage the complementary information present in these modalities to enhance the accuracy of various medical applications. We demonstrate the strength and the generality of our method on two different brain Magnetic Resonance Imaging (MRI) analysis tasks, namely, brain age prediction conditioned by subject's sex, and multiclass Alzheimer's Disease (AD) classification conditioned by tabular data. We show that our framework outperforms both single-modality models and state-of-the-art MRI-tabular data fusion methods. The code, enclosed to this manuscript will be made publicly available.

Keywords: Deep Learning, Hypernetworks, Tabular-Imaging Data Fusion, Multimodal, Alzheimer Diagnosis, Brain Age Prediction

1. Introduction

In medical decision-making, clinicians depend on comprehensive patient information to make precise diagnoses and well-informed decisions.

The refinement and amalgamation of all available data are crucial for personalized healthcare. This is particularly relevant in image-based diagnoses, where the inclusion of clinical and demographic patient information from the Electronic Health Record (EHR) significantly improves diagnostic accuracy.

Deep Neural Networks (DNNs) consistently achieve state-of-the-art results across a broad spectrum of medical tasks. However, they still cannot match human experts' abilities to fuse medical imaging and EHR data, typically presented in tabular format. The main challenge arises from the inherent disparities between these

*Data used in preparation of this article were obtained from the Alzheimer's Disease Neuroimaging Initiative (ADNI) database (adni.loni.usc.edu). As such, the investigators within the ADNI contributed to the design and implementation of ADNI and/or provided data but did not participate in analysis or writing of this report. A complete listing of ADNI investigators can be found at: http://adni.loni.usc.edu/wp-content/uploads/how_to_apply/ADNI_Acknowledgement_List.pdf

two types of data. Images are high-dimensional, continuous, and spatial, while tabular data typically comprise low-dimensional features with diverse types, scales, and ranges. Nevertheless, employing DNNs for this integration offers significant advantages, as they can process extensive volumes of data and extract intricate structural relationships. The proposed research aims to leverage DNNs’ capabilities while addressing the challenges of data fusion through hyper-networks.

When considering multi-modal fusion of imaging and non-imaging data, the integration of images and textual data comes to mind. This well-studied problem has attracted significant attention following its outstanding success (Perez et al., 2018; Anderson et al., 2018; Radford et al., 2021). In the clinical domain, numerous methods have been proposed to combine text and medical imaging (Wang et al., 2022). However, while texts significantly differ from images in terms of structure and dimension, these two sources of data often have explicit semantic relations, as seen in image captions (Vinyals et al., 2015; Xu et al., 2015; Wang et al., 2016), generation of images from text (Zhang et al., 2023, 2018), visual question answering (Perez et al., 2018; Anderson et al., 2018), or radiology interpretation (Dawidowicz et al., 2023; Wang et al., 2022).

Dealing with tabular data, certain measures (typically related to size or morphology) may directly correspond to the scanned anatomy. Recent work by Hager et al. has utilized such correspondences to establish associations between different modalities (Hager et al., 2023). However, numerous other clinical and demographic attributes, including measures obtained in medical laboratory tests, the medical history of patients or their biological relatives, and even years of education, provide complementary information, independent of the imaging data. For example, a chest X-ray may require additional clinical measures (e.g., body temperature) for an accurate diagnosis of pneumonia (Huang et al., 2020). Our goal is to develop a deep learning model capable of enhancing data utilization by extracting implicit, possibly complex correlations between different, modality-specific characteristics.

A straightforward and intuitive approach to fuse image and tabular data involves using separate networks for each data type and making a collective decision based on their outcomes (Prabhu et al., 2022). The processing of each data type typically involves a Multi-Layer Perceptron (MLP) for tabular data and a Convolutional Neural Network (CNN) for imaging. Another common approach entails embedding each modality into a feature vector followed by vector concatenation (Esmailzadeh et al., 2018; El-Sappagh et al., 2020; Venugopalan et al., 2021). Other methods, such as those presented in (Wolf et al., 2022), leverage tabular data to condition image processing through affine transformations in the convolutional layers. In all of these techniques, the interaction between different data types is confined to specific stages of the processing pipeline and specific transformations, potentially limiting the network’s ability to fully exploit the advantages of data fusion.

We present a conceptually innovative approach to the challenge of fusing imaging and tabular data. Specifically, we designate tabular measurements and values as priors influencing the outcomes of the image analysis network. This can be

likened to conditioning the results of the image analysis network on the tabular data, comparable to adjusting the auditory output of a radio transmitter by manipulating frequency (selecting stations) and volume. The central concept is implemented through hypernetworks. Originally introduced by (Ha et al., 2016), the hypernetwork framework comprises a primary network assigned to a specific task and a hypernetwork responsible for generating weights and biases for specific layers in the primary network. This arrangement enables the framework to condition the processing of one modality in the primary network based on information from another modality processed within the hypernetwork. The entire fusion process is akin to finely adjusting the focus of image processing based on attributes present in the tabular data.

We demonstrate the versatility and efficacy of the proposed hypernetwork framework, named HyperFusion, through two distinct brain MRI analysis tasks: brain age prediction conditioned by the subject’s sex and classification of subjects into Alzheimer’s disease (AD), Mild Cognitive Impairment (MCI), and Cognitively Normal (CN) groups conditioned by their tabular data, which includes clinical measurements, as well as demographic and genetic information.

The rest of this paper is structured as follows: In Section 2, we present a literature review on imaging and tabular data fusion. We also delve into the concept of hypernetworks and their applications. Furthermore, we discuss studies related to the brain age prediction and AD classification tasks. Section 3 presents our hypernetwork framework along with details about the architectures designed for each task and key implementation aspects. In Section 4, we describe our experimental setup, including the datasets used and preprocessing steps, as well as training and evaluation procedures. The results of our experiments are presented and discussed in this section as well. We conclude in Section 5.

2. Related Work

2.1. Fusion methods

The emergence of public multi-modal medical imaging datasets and benchmarks have facilitated the development of methods for integrating structural images of different contrasts for enhanced clinical analysis and, in particular, pathology segmentation (Menze et al., 2014; Carass et al., 2017). Recent efforts concentrate on accommodating missing imaging (mainly MRI) modalities during training time and inference, which appears to be a main bottleneck (Yang et al., 2023). Another line of works focuses on the synergy between functional, structural and diffusion images which require additional processing since the voxel values of each modality convey different properties (Sui et al., 2023). However, the incorporation of modalities with no spatial structure, such as tabular data, poses further challenges.

Fusion strategies for combining medical imaging and tabular data can be categorized into three distinct types, as outlined in (Huang et al., 2020): early fusion, where original or extracted features are concatenated at the input level, e.g., (Chierigato et al., 2022); joint fusion (or intermediate fusion), where the

feature extraction phase is learned as part of the fusion model; and late fusion, where predictions or pre-trained high level features are combined at the decision level, as in (Pandeya and Lee, 2021; Prabhu et al., 2022).

In this study, we employ the joint fusion approach to facilitate meaningful interaction between modalities. Due to the inherent disparities between tabular and image data, direct integration is not feasible, necessitating some preprocessing. Early fusion proves inadequate for end-to-end processing, leading to the independent processing of image features and hindering the potential for mutual learning between modalities at the intermediate level. Late fusion, on the other hand, occurs solely at the decision level of trained models, failing to foster mutual learning between modalities. In contrast, joint fusion offers the advantages of end-to-end training as well as the potential to condition modality processing based on each other.

A straightforward joint fusion approach for integrating imaging and tabular data involves concatenating their latent feature vectors, as exemplified in studies such as (Esmailzadeh et al., 2018; El-Sappagh et al., 2020; Venugopalan et al., 2021). In this approach, tabular data or processed tabular features are merged with high-level image features through a fully connected layer or a small MLP, enabling gradient propagation to both tabular and image processing networks. However, methods based on late concatenation may limit the interaction between tabular data and imaging to high-level descriptors, neglecting fusion in convolutional layers where crucial spatial image context is preserved.

A more advanced joint fusion approach operates within the intermediate layers of a CNN by applying an affine transformation to the image features. The shift and scale parameters are generated by a network that processes another data modality. In (Perez et al., 2018), a Feature-wise Linear Modulation (FiLM) was introduced for conditioning image processing on text, applied to a visual question-answering task. Building upon FiLM, (Wolf et al., 2022) introduced the Dynamic Affine Feature Map Transform (DAFT) to fuse brain MRIs and tabular data. We compared our framework to both DAFT and FiLM. It is worth noting that these methods are limited to linear transformations applied exclusively to the convolutional layers.

Addressing a different yet related problem, (Hager et al., 2023) tackles the scenario where tabular data is assumed to be unavailable during the inference phase but can be utilized during training to leverage semantic dependencies within imaging data. The methodology employs contrastive learning to understand imaging-tabular correspondences. However, as highlighted in Section 1, our work observes that the most relevant tabular features are distinctly present in the imaging data. In certain cases, the tabular data encompasses vital attributes that are challenging or nearly impossible to derive from imaging alone, such as specific protein measurements and metabolic indicators. Moreover, it is worth noting that (Hager et al., 2023) relies on extensive datasets for effective contrastive learning utilization, while our work also addresses situations with smaller datasets lacking comprehensive representation. In such instances, explicitly providing information from the tabular data can prove more beneficial than relying on implicit extraction

from the image.

Our work incorporates the concept of conditioning image processing on tabular data by employing a hypernetwork framework. In contrast to other methods, our hypernetwork approach is versatile and comprehensive. Specifically, the proposed hypernetwork learns a general transformation (not necessarily linear) to adapt the parameters transferred to the primary network’s layers, regardless of their architecture or position. This flexibility allows the fusion of imaging with any other modality regardless of the context.

2.2. Hypernetworks

The notion of hypernetworks, where one network (the hypernetwork) generates the weights and biases for another network (the primary network), was introduced in (Ha et al., 2016). We drew inspiration from two distinct applications of hypernetworks, one being the work of (Littwin and Wolf, 2019). This work utilized 2D images input into a hypernetwork for the reconstruction of depicted 3D objects via the primary network. Another inspiring application is found in the denoising framework presented by (Aharon and Ben-Artzi, 2023), where the hypernetwork was trained to generate primary network parameters conditioned by the latent signal-to-noise ratio (SNR) of the input image.

Hypernetworks have found applications in the medical domain as well. In (Wydmański et al., 2023), a hypernetwork framework processes tabular data using random feature subsets. In this context, a random binary mask selects a subset of tabular features, simultaneously serving as the input to the hypernetwork responsible for generating parameters for the features processing network. However, it is important to note that this approach is unimodal, focusing exclusively on tabular data, and lacks integration with imaging data, a key aspect addressed in our work.

To the best of our knowledge, the utilization of hypernetworks for the fusion of different data modalities in the medical domain remains an unexplored area.

To showcase our approach, we selected two brain MRI analysis challenges that can potentially benefit from the fusion of imaging and tabular data: brain age prediction, a regression problem, and multiclass classification, involving categorization into AD, MCI and CN. Further details about these tasks are provided below.

2.3. Brain age prediction

The task of predicting human age based on brain anatomy has garnered significant attention in medical research, driven by the development of AI regression tools and the increasing availability of brain imaging data (Franke and Gaser, 2019; Peng et al., 2021; Lee et al., 2022; Cole and Franke, 2017; Feng et al., 2020; Levakov et al., 2020). Current methods, exclusively based on imaging, demonstrate good prediction accuracy, achieving an average gap of less than three years between the actual chronological age and the predicted brain age of healthy subjects. However, since the primary goal of these studies is neural network explainability, aiming to provide insights into

brain aging dynamics, relying solely on imaging does not capture other attributes that may influence these processes.

Acknowledging the differences in aging trajectories between males and females (Coffey et al., 1998; Piçarra and Glocker, 2023), we explored whether incorporating subject sex information could enhance brain age prediction. To the best of our knowledge, we are the first to address the task of brain age inference conditioned by the subject’s sex. However, it is essential to note that this exploration is a secondary aim of our study. The primary objective is to showcase and demonstrate our proposed hypernetwork framework, specifically focusing on the fusion of imaging and non-imaging data.

2.4. Alzheimer’s disease classification

Early detection of AD from brain MRI is a topic of active research due to its significant implications. The most challenging aspect lies in classifying individuals with MCI, a transitional stage that serves as a potential predictor for the development of AD. Unlike methods designed for binary classification (CN vs. AD), such as those presented in (Bäckström et al., 2018; Wang et al., 2018), our focus is on multi-class classification into CN, MCI, and AD.

While many studies addressing this problem rely on imaging data alone, as seen in (Wen et al., 2020) and related works, neurology-related literature suggests the inclusion of clinical and demographic data for enhanced prediction. For instance, works like (Letenneur et al., 1999; Fratiglioni et al., 1991) highlight differences in the hazard ratio of AD between women and men, as well as among individuals with varying levels of educational attainment. The Alzheimer’s Disease Neuroimaging Initiative (ADNI) dataset offers additional tabular data containing essential attributes and biomarkers for AD detection, such as specific protein measurements in the Cerebrospinal Fluid (CSF) and metabolic indicators derived from Positron Emission Tomography (PET) scans.

These additional attributes and their interactions provide relevant information that may not be present in brain MRI scans alone. In recent years, several multi-modal fusion methods for AD detection have been proposed (Dolci et al., 2022; Venugopalan et al., 2021; El-Sappagh et al., 2020; Zhou et al., 2019; Liu et al., 2018; Spasov et al., 2018). In this manuscript, we specifically refer to (Wolf et al., 2022; Esmailzadeh et al., 2018; Prabhu et al., 2022), which addressed the fusion of MRIs and tabular data from the ADNI dataset for three-class AD classification.

3. Method

3.1. HyperFusion

The proposed deep learning framework aims to integrate imaging and tabular data to enhance clinical decision-making. Figure 1 describes its two main building blocks: a hypernetwork denoted by \mathcal{H}_ϕ and a primary network \mathcal{P}_θ , where ϕ and θ represent their respective parameters. For simplicity, we denote the entire network compound as $\mathcal{F} = \{\mathcal{H}_\phi, \mathcal{P}_\theta\}$.

The input to \mathcal{F} consists of a paired tabular vector of d measurements/values $T \in \mathbb{R}^d$ and a multidimensional image I ,

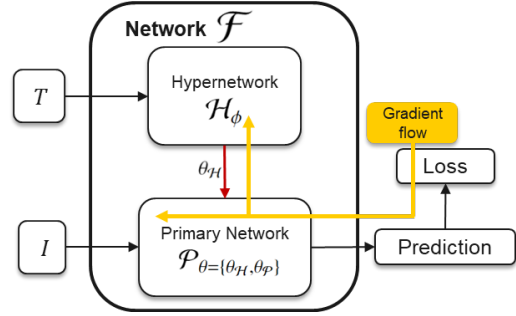


Figure 1: **A general overview of the proposed hypernetwork framework.** The proposed framework (\mathcal{F}) consists of a hypernetwork (\mathcal{H}_ϕ) and a primary network (\mathcal{P}_θ), where ϕ and θ denote the parameter sets for \mathcal{H} and \mathcal{P} , respectively. The primary network parameters θ are divided into external parameters $\theta_{\mathcal{H}}$ generated by the hypernetwork and internal parameters $\theta_{\mathcal{P}}$ which are learned throughout the backpropagation process. The inputs to \mathcal{F} include the tabular data T which are fed into the hypernetwork and the imaging data I which are fed into the primary network. The entire network compound is trained in an end-to-end manner where the gradients flow through the primary network layers to the hypernetwork layers updating both $\theta_{\mathcal{P}}$ and ϕ simultaneously. The external primary network parameters $\theta_{\mathcal{H}}$ are not directly affected by the backpropagation process.

specifically, a 3D MRI. Given a tabular vector T , \mathcal{H} produces a data-specific set of network parameters $\theta_{\mathcal{H}} = \mathcal{H}_\phi(T)$, which, combined with internally learned parameters $\theta_{\mathcal{P}}$, forms the entire set of primary network parameters $\theta = \{\theta_{\mathcal{H}}, \theta_{\mathcal{P}}\}$. The output of the primary network $\mathcal{P}_\theta(I)$ represents the desired clinical prediction. During the training phase, the loss backpropagates through both the primary and hypernetwork, influencing both $\theta_{\mathcal{P}}$ and ϕ . Notably, the external primary network parameters $\theta_{\mathcal{H}}$ are updated indirectly. This structure allows us to condition the image analysis on the tabular data.

Figure 2 provides a detailed view of the proposed architecture and flow. The input image (Figure 2A) is fed into the primary network \mathcal{P}_θ (Figure 2C), a CNN. Simultaneously, the tabular data input (Figure 2A) is processed by the hypernetwork \mathcal{H}_ϕ (Figure 2B), composed of K sub-networks $\{h_k\}_{k=1,\dots,K}$, each embeds the tabular attributes (see Section 3.1.1) and generates weights and biases $h_k(T) = \theta_{h_k}$ for a corresponding layer in the primary network \mathcal{P}_θ . These external parameters of the primary network’s layers depend on T and influence the extracted imaging features accordingly.

The dependency on tabular data is determined by the ratio between external and internal parameters. To gain insights, let’s examine two edge cases. When relying solely on internal network parameters (without a hypernetwork), predictions become indifferent of the tabular information. Conversely, the case where all primary network parameters are external and generated by the hypernetwork, approximates a scenario where separate networks are employed for each combination of tabular attributes. For instance, in brain age prediction, the hypernetwork might generate different parameter sets for men and women. However, while there will be some dependencies thanks to the embedding (Section 3.1.1), having all parameters external would probably necessitate an extended training process with a higher amount of training data. In our configurations, we opted for parameters of low-level primary network layers to be internal, assuming that tabular attributes (e.g., sex) are less likely

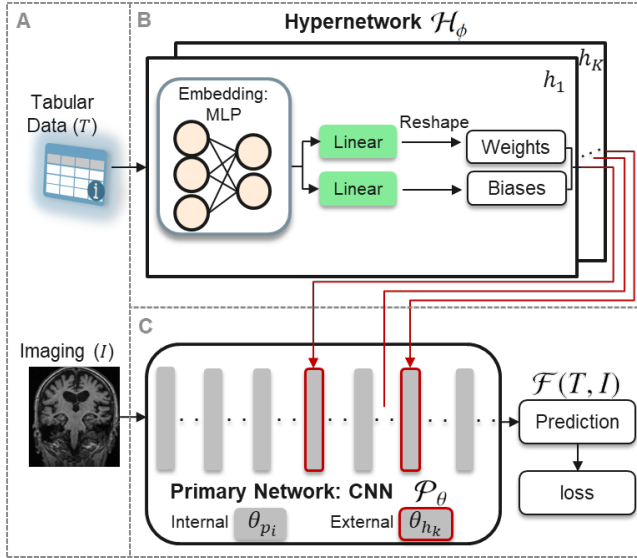


Figure 2: A detailed illustration of the proposed HyperFusion’s network compound \mathcal{F} . A: The inputs T and I denote tabular and imaging data, respectively. The images I can be of any type or dimension (in this study we used 3D MRI scans). The tabular data $T \in \mathbb{R}^d$ have d attributes. B: The hypernetwork \mathcal{H}_ϕ is composed of K individual networks, $\{h_k\}_{k=1,\dots,K}$, which generate parameters $h_k(T) = \theta_{h_k}$ for specific layers of \mathcal{P}_θ . Each h_k is composed of an MLP embedding network and two linear layers for converting the latent tabular data vector into weights and biases, which are then reshaped to suit their respective mathematical operations in \mathcal{P}_θ . C: The primary network \mathcal{P}_θ is a CNN designed for processing the imaging data. The parameters of the primary network \mathcal{P}_θ , is composed of $\theta_{\mathcal{H}} = \{\theta_{h_k}\}_{k=1,\dots,K}$ and $\theta_{\mathcal{P}} = \{\theta_{p_i}\}_{i \in L}$, where L represents the collection of indexes for layers that are not directly connected to the hypernetwork. The parameters of a specific subset of the primary network’s layers (framed in red) are determined by the hypernetwork. These are the external primary network parameters θ_{h_k} . The other primary network parameters θ_{p_i} are internal and are directly updated throughout the backpropagation process.

to be relevant for the extraction of the low level imaging features that eventually contribute to the prediction. This chosen combination of parameter sources allows us to maximize the utilization of available training scans while incorporating the corresponding tabular data for additional gains.

3.1.1. Embedding the tabular data

As depicted in Figure 2B, the proposed hypernetwork generates weights and biases in a two-step process. Initially, the tabular data is input into an embedding network, resulting in a latent vector. Subsequently, this latent vector passes through two distinct linear layers: one for generating weights and another for generating biases. Let $\zeta: \mathbb{R}^d \rightarrow \mathbb{R}^l$ define the embedding function, mapping the tabular data T into a lower dimension space ($l < d$). The desired embedded feature vectors should have a condensed, meaningful representation of the original data, aiming to capture hidden patterns and intricate interactions, while preserving the relevant information. The embedding is a critical step in the fusion process, offering complex associations to the tabular data.

For our tabular embedding network, we opted for an MLP model given that tabular data lacks spatial context. This choice aligns with its favorable performance and suitability for small datasets, as noted in (Borisov et al., 2022). However, the hypernetwork configuration remains versatile, allowing the integra-

tion of any desired embedding architecture.

The proposed framework is end-to-end and the embedding parameters are learned concurrently with the entire network, as illustrated in Figures 1 and 2B. Moreover, the continuity of the embedding space, where similar samples are mapped closer together, enables interpolation. This capability allows the model to generate meaningful representations for previously unseen samples, enhancing its ability for generalization

3.1.2. Weights initialization

A network’s convergence is contingent upon the initial distribution of its parameters. Typically, neural network layer parameters are initialized with consideration to their fan-in or fan-out, a practice that stabilizes their convergence, as outlined in (He et al., 2015a; Glorot and Bengio, 2010). In our context, parameter initialization assumes a crucial role, particularly concerning $\theta_{\mathcal{H}}$ generated by the hypernetwork (its output) for the primary network. These parameters are computed as part of the hypernetwork’s feedforward process and cannot be directly initialized to follow a specific distribution. Furthermore, these parameters vary with each different input sample T .

To address this challenge, we employed the technique detailed in (Chang et al., 2019), which conducted variance analysis on the hypernetwork’s output, $\theta_{\mathcal{H}}$. The method aims to initialize the internal hypernetwork parameters (ϕ) in a way that enables the feedforward process of the hypernetwork to generate external primary network parameters (θ_{h_i}) fitting a specific distribution. More precisely, the distribution of these parameters should ensure that the output variance in their designated layers within the primary network closely aligns with the input variance. This initialization contributes to the convergence of the proposed hypernetwork framework.

3.2. Loss functions

As depicted in Figure 1 the loss backpropagates throughout the entire network compound affecting both the internal primary network’s parameters and the hypernetwork. Given the flexibility of our framework, the loss function can be adapted to a wide range of applications. It consists of two components the task-specific loss, $\mathcal{L}_{\text{task}}$, and a weight decay regularization term $\mathcal{L}_{\text{regularization}}$ as follows:

$$\mathcal{L}(y, \mathcal{F}(T, I)) = \mathcal{L}_{\text{task}}(y, \mathcal{F}(T, I)) + \mathcal{L}_{\text{regularization}}(\{\phi, \theta_{\mathcal{P}}\}), \quad (1)$$

where, y are the true labels/values. The regularization is applied to ϕ and $\theta_{\mathcal{P}}$ to reduce overfitting. Recall that the external primary network parameters produced by the hypernetwork, i.e., $\theta_{\mathcal{H}}$ do not go through the gradient descent process and therefore are not regularized.

The loss term $\mathcal{L}_{\text{task}}$ in regression tasks is the Mean Square Error (MSE) between the predictions \hat{y} and the ground truth values as follows:

$$\mathcal{L}_{\text{task} = \text{regression}}(y, \hat{y}) = \frac{1}{B} \sum_{i=1}^B (y_i - \hat{y}_i)^2 \quad (2)$$

where B is the batch size and i is the sample index.

For classification tasks with C classes, aiming to account for potential class imbalance, we use the Weighted Cross-Entropy (WCE) loss. The weight of each class c is denoted as w^c , and is inversely proportional to the frequency of the class in the training and validation sets. The WCE loss is formulated as follows:

$$\mathcal{L}_{\text{task = classification}}(\mathbf{P}, \hat{\mathbf{P}}) = - \sum_{i=1}^B \sum_{c=1}^C w^c p_i^c \log(\hat{p}_i^c) \quad (3)$$

where, p_i^c and \hat{p}_i^c denote the ground truth and the predicted probability of class c , respectively, and \mathbf{P} and $\hat{\mathbf{P}}$ are the batched ground truth (one hot) and the predicted distributions.

3.3. Missing values

It is not uncommon to have tabular data with missing values. Handling missing values is a crucial aspect of tabular data pre-processing, as it can significantly impact the quality of modeling and analysis. There exist different strategies to address this challenge. For example, the multi-modal generative approach proposed in (Dolci et al., 2022) which compensates for missing modalities via a three-module framework. In the first module, each modality is processed independently, the second one imputes the unavailable data using pretrained generators and the last module fuses all features prior to the prediction.

In our study, we impute missing values using an iterative approach. The tabular data is presented as a matrix where each column represents an attribute and each row is a training set sample. In each step, one attribute (column) is selected as the output z , and the remaining columns are considered as inputs X . A regressor is trained on the non missing values of (z, X) , and then employed to predict the missing values of z . This iterative process repeats for each of the columns. As in (Wolf et al., 2022) we add a indicator, such as a NaN flag to indicate imputed values.

While this technique is widely used, it is important to acknowledge potential biases it may introduce. Often, the values of specific attributes are consistently absent from datasets which belong to specific classes. For instance, datasets related to CN subjects typically lack measurements that might pose health risks, requiring invasive procedures or imaging with ionizing radiation. In such cases, the presence of an indicator for missing values could itself be an 'unfair' cue, potentially leading to improved results for the 'wrong reasons'. Additionally, the imputation of attributes with missing values in datasets related to one class might heavily rely on the existing values of another class, potentially compromising their validity. Despite these concerns, we opted for the imputation strategy outlined above to ensure a fair comparison with existing methods that utilize it.

3.4. Ensemble learning

To enhance and stabilize the inference process, we use an ensemble model, denoted as \mathcal{E} , which aggregates the results of M trained models, \mathcal{F}_1 to \mathcal{F}_M . Addressing regression problems, the final prediction is a simple average of the predictions provided by all ensemble's models:

$$\mathcal{E}_{\text{regression}}(T, I) = \frac{1}{M} \sum_{m=1}^M \mathcal{F}_m(T, I). \quad (4)$$

In multiclass classification tasks involving C classes, each model \mathcal{F}_m produces a probability distribution vector over the predicted classes, represented as $\mathbf{p}_m = (p^{c=1}, \dots, p^{c=C})_m$. To obtain the final ensemble prediction, $\mathcal{E}_{\text{classification}}(T, I)$, these models are combined using the weighted average of their probability distributions, as follows:

$$\mathcal{E}_{\text{classification}}(T, I) = \sum_{m=1}^M w_m \mathcal{F}_m(T, I) = \sum_{m=1}^M w_m \mathbf{p}_m. \quad (5)$$

Here w_m defines the weight of the prediction of \mathcal{F}_m in the ensemble. In general, we wish w_m to be higher for models with higher confidence (lower uncertainty). Assuming that the prediction uncertainty positively correlates with its entropy, we set w_m to be inversely proportional to the entropy of network's prediction, as follows:

$$w_m = \frac{J(\mathcal{F}_m(T, I))}{\sum_{i=1}^M J(\mathcal{F}_i(T, I))} = \frac{J(\mathbf{p}_m)}{\sum_{i=1}^M J(\mathbf{p}_i)}, \quad (6)$$

where $J(\cdot)$ is defined by $\frac{1}{H}$ and H is the entropy function. The term $\sum_{i=1}^M J(\mathbf{p}_i)$ serves as a normalization factor.

3.5. Imaging-tabular data fusion applications

To showcase the versatility of the proposed imaging-tabular data fusion framework, we explore two distinct medical imaging applications, each featuring a unique architectural configuration. These applications encompass brain age prediction conditioned by the subject's sex (Section 3.5.1) and multi-class classification of subjects into AD, MCI, and CN groups (Section 3.5.2).

3.5.1. Conditioned brain age prediction using hypernetworks

The proposed hypernetwork framework for conditioned brain age prediction is illustrated in Figure 3. The primary network takes 3D brain MRI scans (T1w) of healthy subjects as input, while the tabular data fed into the hypernetwork consists of binary values indicating the subjects' sex.

The hypernetwork compound is trained to address a regression problem using the loss function defined in Equations 1 and 2. The primary network architecture (Figure 3B-C) is built upon the VGG backbone (Simonyan and Zisserman, 2014), as suggested in (Levakov et al., 2020) for brain age prediction.

The hypernetwork itself consists of a simple linear layer that embeds the incoming binary tabular data through a 2-to-1 layer configuration, as depicted in Figure 3D. The embedding step is crucial, especially when using the orthogonal one-hot representation of the sex attribute (01 or 10). Without embedding, the hypernetwork would generate a distinct set of weights for each sex attribute value. We found that in this case, the most effective integration of the hypernetwork occurred within the linear layers at the final processing stage.

3.5.2. AD classification using hypernetworks

Figure 4 visually presents the hypernetwork framework for multi-class classification of subjects into CN, MCI, and AD groups. The input to the hypernetwork (Figure 4A) is the

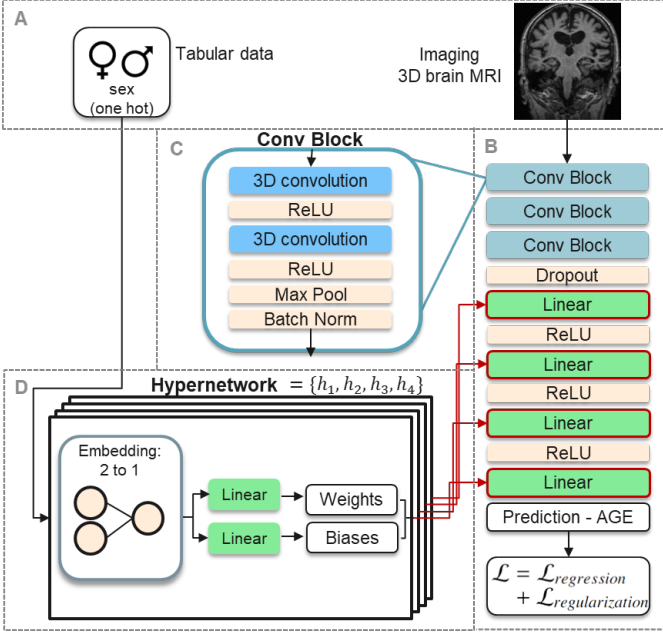


Figure 3: The proposed HyperFusion architecture for the conditioned brain age prediction task. A: The inputs include the subjects’ sex (encoded as a 2D one-hot vector) representing a single attribute tabular data and the corresponding 3D brain MRIs. B: The primary network backbone is a variant of the VGG architecture (Simonyan and Zisserman, 2014), where the parameters of its final four linear layers (framed in red) are external and generated by the hypernetwork. The network output the subjects’ brain age ($\in \mathbb{R}$), and the loss function is a weighted sum of the regression loss (MSE) and weight decay regularization, as defined in Equations 1-2. C: A closer look of a convolutional block, comprising two convolutional layers with ReLU activation, batch normalization and downsampling through max-pooling. D: The hypernetwork comprises four sub-networks (h_1, h_2, h_3, h_4), each corresponds to one of the linear layer in the primary network. Each h_k is composed of a 2-to-1 MLP for the embedding of the one-hot input vectors.

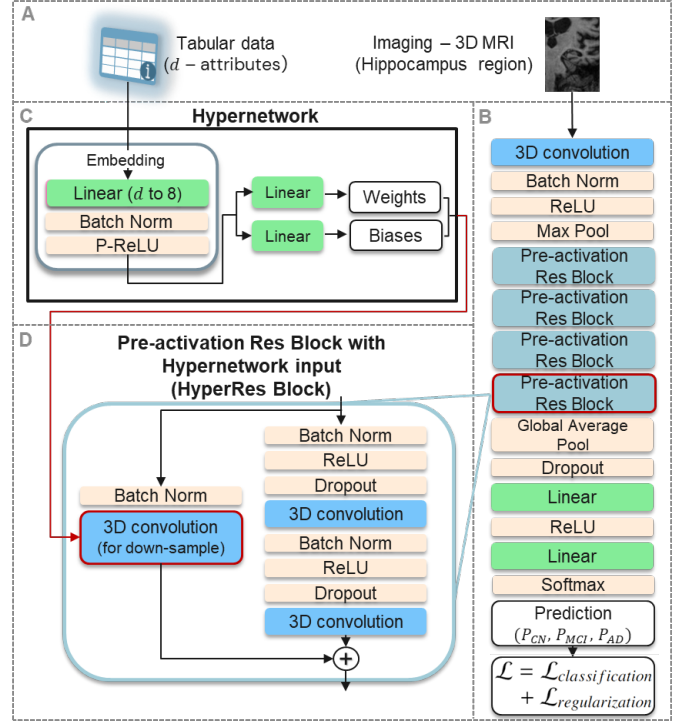


Figure 4: **The proposed HyperFusion architecture for the AD classification task.** A: The input to the network compound include clinical and demographic tabular attributes (d in total) of the subjects along with their brain MRIs. B: The primary network’s is composed of pre-activation ResNet blocks followed by two linear layers. The last ResNet block (HyperRes block, framed in red) gets a subset of its parameters from the hypernetwork. The primary network predictions are probability distributions (P_{CN}, P_{MCI}, P_{AD}) produced by the softmax layer. The loss is a weighted sum of the classification loss (weighted CE) and weight decay regularization, as detailed in Equations 1,3. C: The hypernetwork is composed of an MLP for embedding, with Parametric ReLU (P-ReLU) (He et al., 2015b). The MLP generates weights and biases for the primary network. D: A closer look at the pre-activation Res Block. The architecture (based on (He et al., 2016)) is the same for all blocks, yet the illustration specifically refers to the HyperRes block which gets the parameters to its convolutional layer (framed in red) from the hypernetwork.

tabular data which comprise nine clinical and demographic attributes as described in Section 4.2.3. Similar to the brain age prediction’s application, the primary network is fed with 3D brain MRI scans (Figure 4B). Yet, for AD classification, the images were cropped to include only the hippocampus and its surrounding tissues as suggested in (Wen et al., 2020). The cropping significantly reduced the input size leading eventually to a reduction in the number of the required network parameters and to better classification results. We note that the hippocampus is the significant component of the limbic lobe being a crucial region for learning and memory. Hippocampal atrophy is a known bio-marker for AD (Rao et al., 2022; Salta et al., 2023). The hypernetwork, illustrated in Figure 4C is composed of a non-linear, single-layer MLP used for embedding, with Parametric ReLU (P-ReLU) (He et al., 2015b). The MLP generates weights and biases for the primary network. The primary network predictions are probability distributions (P_{CN}, P_{MCI}, P_{AD}) produced by the softmax layer. The loss is a weighted sum of the multi-class classification loss (WCE) and a weight decay regularization term, as detailed in Equations 1,3. The backbone of the primary network, depicted in Figure 4B is based on the pre-activation ResNet blocks followed by two linear layers. The last ResNet block (framed in red), called the HyperRes block, gets a subset of its parameters from the hypernetwork.

A closer view of a pre-activation ResNet blocks is presented in Figure 4D. The architecture (based on (He et al., 2016)) is the same for all blocks, yet the illustration specifically refers to the HyperRes block which gets the parameters to one of its convolutional layer (framed in red) from the hypernetwork.

4. Experiments

In this section, we elucidate the experimental configurations, ablation studies, prediction outcomes, and comparisons for two diverse brain imaging analysis applications, aiming to showcase the robustness and adaptability of the proposed multi-modal fusion hypernetwork framework. In particular, Section 4.1 delves into the experiments and findings related to brain age estimation conditioned by the subject’s sex, while Section 4.2 addresses multi-class classification of subjects into CN, MCI, or AD groups.

4.1. Brain age prediction conditioned by sex

While most existing approaches address brain age estimation based on brain MRI data alone, we condition the brain age regression problem on the subject’s sex. We first validate the hypothesis that sex information improves the accuracy of brain age prediction. We then evaluate the efficiency of the hyper-network framework in fusing imaging and tabular data. This evaluation involves a comparison with the baseline model that exclusively relies on brain MRI data.

4.1.1. The data

The data for this study include 26,691 brain MRI scans of different healthy human subjects from 19 sources. The table in Appendix A presents a comprehensive information on each dataset including the number of subjects as well as their age and sex distributions.

4.1.2. Preprocessing and partitioning

We applied a preprocessing pipeline to the T1-weighted MRI scans as proposed in (Levakov et al., 2020) - see Appendix A for details. Before being utilized as model inputs, the images were standardized to attain a mean of zero and a standard deviation of one across all non-zero voxels, ensuring data uniformity for an effective training. We note that subjects’ sex and age are routinely recorded during the scanning visits. Therefore we can utilize almost all of the available scans without having to handle issues related to missing values. The tabular data, in this case, consists of a single binary value which is the subject’s sex - male or female. It is represented in our study by a 2D one-hot vector. We partitioned the dataset into training (80%), validation (10%), and test (10%) subsets, preserving consistent age and sex distributions across all the subsets.

4.1.3. Differences in brain aging between males and females

Prior to demonstrating the strength of the proposed hyper-network integrating imaging and tabular data for the task of brain age prediction conditioned by the subject’s sex we conducted a baseline experiment to support the assumption that the availability of sex information enhances the prediction results. We trained three CNNs, each tailored to a specific dataset: one dedicated to male brain scans, another to female brain scans, and a third to mixed data encompassing both sexes. The mixed dataset, comprising approximately half the volume of the complete dataset, ensured equitable sample representation for each model during training, facilitating a fair comparison. Our evaluations encompassed the entire test set, as well as two subsets—one exclusively featuring male subjects and the other exclusively featuring female subjects.

The results of this experiment assessed our hypothesis (Figure 5A): Models that were trained on single sex data achieved the highest performance on test data acquired from the people of the corresponding sex (among all three models) Confirming the validity of our hypothesis enables us to proceed and incorporate the hypernetwork.

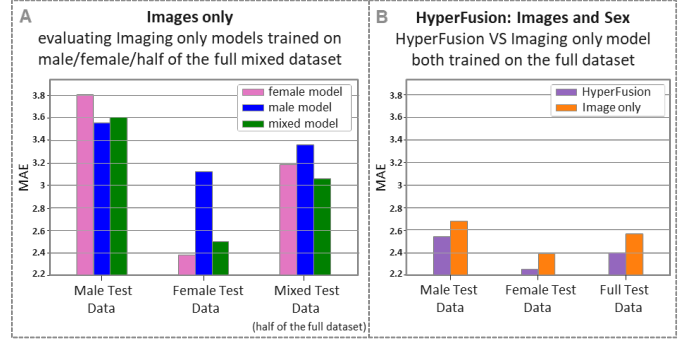


Figure 5: Conditioned brain age prediction results. A) An imaging only experiment. A presentation of the MAE for baseline networks trained on either male only (blue), female only (pink) and mixed (green) equally sized training sets, where the test sets are composed of male only (left), female only (middle) or mixed (right) subsets. The plot demonstrate that when a network is trained and tested on a same-sex population the MAE results are enhanced, assessing the hypothesis that aging processes are influenced by the subjects’ sex. B) HyperFusion: Images and Sex. A comparison between the baseline model (orange) using imaging data alone and the proposed HyperFusion model (purple) exploiting both imaging data and sex information in terms of MAE. The test was performed using either males subset (left), females subset (middle) or the full dataset (right).

4.1.4. Training and evaluation

We used the Mean Average Error (MAE) between the chronological and the predicted age for evaluating our framework. To ensure robustness, we trained multiple models with different random weight initialization mitigating the potential impact of incidental results. The test results were calculated based on an ensemble of the five highest-performing models identified during validation. The ensemble’s output was derived through an average of the models predictions, as detailed in Section 3.4, further enhancing the reliability of our findings.

4.1.5. Results and discussion

A comparison of the hypernetwork framework to the training of two separate networks each with approximately half the data (either males or females) clearly demonstrates that the HyperFusion enables a much more efficient data utilization. Integrating information from subjects of both sexes, the hypernetwork enhanced the prediction accuracy as shown in Figure 5B. Although not within the scope of this paper, it is interesting to note that female data age prediction is much more accurate than male age prediction (see left-most and middle bars in Figure 5A and B). This could be derived from the higher variability of age related brain appearance in males.

4.2. Alzheimer’s disease classification

To further assess the efficiency of our network in fusing imaging and tabular data, we conducted a set of experiments on the AD classification task conditioned by different number and compositions of tabular data attributes. We compared our results to those obtained using either of the data modalities as well as to other existing approaches.

4.2.1. The data

We used four phases of the ADNI database (ADNI1, ADNI2, ADNI GO, and ADNI3) and sorted out datasets of 2120 sub-

Table 1: Statistics on the CN, MCI and AD groups in our data. Information includes the number of samples "N" per label, the mean and standard deviation of age, and the male/female ratio within each diagnostic group

Diagnosis	N (%)	Age - mean (\pm std)	Sex (M:F)
AD	365 (17.2%)	75.1 (\pm 7.8)	(198:167)
CN	740 (34.9%)	72.2 (\pm 6.8)	(309:431)
MCI	1015 (47.9%)	72.8 (\pm 7.6)	(569:446)
Over all	2120 (100%)	73.0 (\pm 7.4)	(1076:1044)

jects. Since part of the ADNI data is longitudinal we excluded part of the data to ensure each subject has a single, yet complete, visit’s dataset, i.e., a single MRI scan and the (temporally) corresponding EHR. Statistics of the ADNI data used are presented in Table 1. The concrete imaging and EHR datasets we used along with the corresponding ADNI’s subject identification numbers are available at the Git repository enclosed to this work.

4.2.2. Image preprocessing

The preprocessing pipeline of the MRI scans is similar to the one in Section 4.1.1. As discussed in Section 3.5.2, we cropped the scans into two 3D sub-images of size $64 \times 96 \times 64$ voxels, including either the left or the right hippocampus regions.

4.2.3. Tabular preprocessing

While the subjects’ EHRs contain numerous attributes we chose to use only nine of them. The demographic attributes include age, sex, and education. The CSF biomarkers include $A\beta$ 42, P-tau181, and T-tau. The third attribute category encompasses composite measures derived from 18F-fluorodeoxyglucose (FDG) and florbetapir (AV45) PET scans. It is important to note that cognitive scores from the EHR were excluded from our study because they were directly used for AD diagnosis. In other words, these scores alone are sufficient for AD classification (Qiu et al., 2018), rendering the entire study meaningless.

Binary (sex) and other discrete attributes were transformed into one-hot vectors. Conversely, attributes with continuous values were centralized and normalized to have zero mean and standard deviation of one. Missing values were handled as described in Section 3.3.

4.2.4. Data partitioning

The dataset is partitioned into five non-overlapping subsets of equal size, ensuring that each subset maintains a similar joint distribution of age, sex, and diagnosis, in accordance with the methodology outlined by (Wen et al., 2020). Among these five subsets, four are allocated for cross-validation, while the fifth is set aside for testing, as depicted in Appendix B. The partitioning involves a random shuffling of the data using a predefined random seed, referred to as the split seed. This systematic approach to data splitting enhances the validity and generality of the evaluation process, showcasing the robustness of our model.

4.2.5. Ablation study and comparisons

To evaluate the effectiveness of our proposed HyperFusion approach for image-tabular data fusion, we conducted a comprehensive analysis comparing it with numerous unimodal and

multi-modal models. The unimodal models include a baseline MLP designed for tabular data and a pre-activation ResNet optimized for image data processing. Both the baseline MLP and the ResNet are components in our complete hypernetwork compound, as illustrated on the left-hand side of Figure 4C and Figure 4B, respectively.

The imaging-tabular fusion models we compared include various methods. The first one, dubbed ‘concatenation’, involved employing our pre-activation ResNet backbone (presented in Figure 4B) yet, replacing the HyperRes block with a regular pre-activation Res block. The tabular attributes were concatenated with the second-to-last fully connected layer, a technique documented in prior works like (Esmailzadeh et al., 2018).

Additionally, we compared our method to the results reported for two contemporary imaging-tabular fusion techniques: the DAFT (Wolf et al., 2022) and the late-fusion approach proposed by (Prabhu et al., 2022). To ensure a fair comparison and highlight the unique (isolated) contribution of our hypernetwork, we constructed and trained two additional networks. Specifically, we utilized our primary network backbone and training regimen, including our proposed regularized weighted categorical loss function, maintaining the methodologies of the FiLM (Perez et al., 2018) (FiLM-like implementation) and the DAFT (Wolf et al., 2022) (DAFT-like implementation). We note our implementation of the FiLM was adapted from (Wolf et al., 2022), since originally the FiLM was designed for text and natural image fusion.

4.2.6. Training and evaluation

We utilized the Adam optimizer for training, coupled with a regularized weighted cross-entropy loss (Equations 1, 3), as outlined in Sections 3.2 and 3.5.2. The embedding MLP, discussed in detail in Section 3.5.2 and depicted in Figure 4C, underwent pre-training exclusively with the training tabular data to expedite the convergence of the entire network compound.

As mentioned in Section 3.5.2, each subject’s imaging data includes two 3D subimages of the left and right hippocampus. During training, we augmented the dataset by randomly selecting either subimage in each feed-forward iteration. For improved predictions during validation and testing, we processed each subject’s data twice, once for each brain side, and averaged the soft decisions. Furthermore, we achieved enhanced test results by employing an ensemble model, as elaborated in Section 3.4.

To guarantee the robustness of our findings, we adopted an extensive cross-validation strategy encompassing three unique split seeds, each undergoing three rounds of random initialization (versions). In every cross-validation iteration, four models were trained and validated on distinct data folds. For effective result utilization, the four models from a specific version and split seed were aggregated to assess their collective performance on a shared, unseen test set. A visualization for better understanding the training, validation, and testing processes is provided in a figure at Appendix B.

We employed various metrics to assess the performance of our framework and compare it with other models. These met-

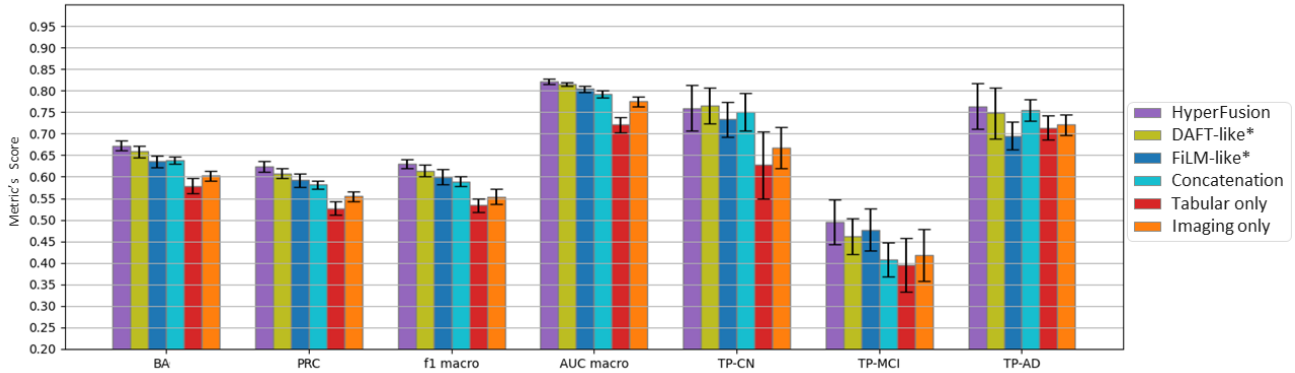


Figure 6: Bar plot presentation of the AD classification results for six competing models and ours using seven different metrics (Section 4.2.6). As previously noted, we included the TP (True Positive) rate for each class as a metric, namely CN (Cognitively Normal), MCI (Mild Cognitive Impairment), and AD (Alzheimer’s Disease). The metrics are represented along the X-axis, with each metric featuring a set of bars corresponding to all competing models. The Y-axis presents the scores achieved by each model for each metric. The bars present the mean and standard deviation over the test data in all random splits and versions. The compared methods including ‘DAFT-like*’ and ‘FiLM-like*’ are described in Section 4.2.5.

Table 2: AD classification results for the proposed method and other competing models. The table presents a comparison of the AD classification task using the HyperFusion method (first row) with respect to baseline methods using either tabular data (second row) or imaging data (third row) alone. The results of a straightforward imaging-tabular concatenation strategy, as well as our improved implementation of the DAFT-like and the FiLM-like models are presented in the 4-th, 5-th and 6-th rows respectively. The last rows present reported results of the late-fusion method of (Prabhu et al., 2022) and the DAFT (Wolf et al., 2022). The comparison is based on seven metrics detailed in Section 4.2.6. As previously noted, we included the TP (True Positive) rate for each class, namely CN (Cognitively Normal), MCI (Mild Cognitive Impairment), and AD (Alzheimer’s Disease). For our method and our implementation of other models we report the mean and standard deviation over the test data in all random splits and versions. In addition, for each metric we calculated the p-value from a Mann-Whitney U test comparing our method to the others to assess the statistical significance of the differences.

model	BA	PRC	f1 macro	AUC macro	TP-CN	TP-MCI	TP-AD
Imaging only	0.579 ± 0.018 p < 0.01	0.527 ± 0.016 p < 0.01	0.534 ± 0.016 p < 0.01	0.721 ± 0.018 p < 0.01	0.627 ± 0.078 p < 0.01	0.395 ± 0.063 p < 0.01	0.714 ± 0.028 p < 0.01
Tabular only	0.602 ± 0.011 p < 0.01	0.555 ± 0.011 p < 0.01	0.554 ± 0.018 p < 0.01	0.775 ± 0.011 p < 0.01	0.668 ± 0.048 p < 0.01	0.418 ± 0.060 p < 0.01	0.721 ± 0.024 p < 0.01
Concatenation	0.638 ± 0.008 p < 0.01	0.582 ± 0.009 p < 0.01	0.589 ± 0.011 p < 0.01	0.792 ± 0.008 p < 0.01	0.751 ± 0.044 p = 0.550	0.408 ± 0.039 p < 0.01	0.755 ± 0.025 p = 0.296
FiLM-like implementation*	0.635 ± 0.014 p < 0.01	0.592 ± 0.016 p < 0.01	0.600 ± 0.017 p < 0.01	0.804 ± 0.007 p < 0.01	0.733 ± 0.040 p = 0.197	0.477 ± 0.049 p = 0.234	0.696 ± 0.032 p < 0.01
DAFT-like implementation*	0.658 ± 0.014 p < 0.01	0.608 ± 0.012 p < 0.01	0.614 ± 0.014 p < 0.01	0.815 ± 0.005 p < 0.01	0.765 ± 0.041 p = 0.717	0.462 ± 0.042 p = 0.038	0.748 ± 0.060 p = 0.224
HyperFusion	0.673 ± 0.012	0.624 ± 0.012	0.630 ± 0.011	0.822 ± 0.006	0.759 ± 0.053	0.495 ± 0.052	0.764 ± 0.052
Reported DAFT results (Wolf et al., 2022)	0.622 ± 0.044	-	0.600 ± 0.045	-	0.767 ± 0.080	0.449 ± 0.154	0.651 ± 0.144
Reported late-fusion results (Prabhu et al., 2022)	0.6330	0.6473	0.6240	-	-	-	-

*our adapted implementation as described in Section 4.2.5

rics include balanced accuracy (BA) and precision (PRC), defined as follows:

$$BA = \frac{1}{3} \sum_c \frac{TP_c}{TP_c + FN_c} \quad PRC = \frac{1}{3} \sum_c \frac{TP_c}{TP_c + FP_c} \quad (7)$$

Here, $c \in \{CN, MCI, AD\}$, and TP_c , FN_c , FP_c represent the True Positive, False Negative, and False Positive values of class c , respectively. Additionally, we utilized the macro Area Under the ROC Curve (AUC) and macro F1 score. A macro AUC/F1 score is the arithmetic mean of all per-class AUC/F1 scores. These metrics consider the global performance of the models. For class-specific assessment of each model we also used the True Positive (TP) rate of each class (TP-CN, TP-MCI, TP-AD). Comprehensive confusion matrices are presented in Appendix C for a thorough evaluation.

4.2.7. Results and discussion

In this section, we conduct a comprehensive comparison between all the models discussed in Section 4.2.5 and our hyper-network model, assessing both global and class-specific metrics. The results are summarized in Table 2 and Figure 6. It is noteworthy that all multi-modal methods consistently outperformed unimodal models in terms of global performance metrics and in nearly all class-specific metrics.

Table 2 presents the reported scores for DAFT (Wolf et al., 2022) and a late fusion method (Prabhu et al., 2022) for certain metrics, along with the results obtained for the methods implemented by us as described in Section 4.2.5. For a fair evaluation of the comparison, we note the following differences.

The late fusion method of (Prabhu et al., 2022) used datasets of 3,256 subjects (35.4% CN, 51.1% MCI, 13.5% AD) from the same ADNI phases that we utilized. The tabular data contained

an extensive set of 20 attributes, including patient demographics, medical history, vital signs, neurophysiological test results, cognitive function, and other relevant diagnostic information. Some of these attributes were deliberately excluded from our study, as noted in 4.2.3. Notably, the late fusion method obtained higher PRC scores at the expense of weaker BA results due to the inherent trade-off between these two metrics using imbalanced datasets. By applying class weight adjustments to the loss function during training, we were able to achieve better PRC and BA compared to the reported late fusion method results, despite using fewer subjects and a smaller set of tabular attributes (results are shown in the Appendix D). The reported DAFT method (Wolf et al., 2022) used datasets of 1,341 subjects (40.3% CN, 40.1% MCI, 19.6% AD) from the same ADNI source and a similar set of tabular attributes. To address the difference in the data size, we presented the scores obtained using our implementation of a DAFT-like method (Section 4.2.5) as well.

Overall, the scores obtained for both global and class-specific metrics in comparison to other unimodal as well as multi-modal fusion methods demonstrate the superiority of the proposed hypernetwork framework. The p-values, calculated from the Mann-Whitney U tests, assess the statistical significance of the differences between the results.

5. Discussion and Conclusions

We introduced hypernetworks as a solution to the intricate task of integrating tabular and imaging data. Additionally, we illustrated how these networks can condition the analysis of patients' brain MRIs based on their EHR data. This interaction between imaging and tabular information enhances the understanding of medical data, facilitating a comprehensive diagnostic process.

The robustness and generality of our method were validated through two distinct clinical applications. The core concepts proposed are adaptable to different network architectures. Furthermore, the straightforward integration of pre-trained networks into our framework promises accelerated convergence and heightened accuracy. Altogether, these aspects position our method as a practical and versatile tool for data fusion.

Our hypernetwork approach surpasses models relying solely on either imaging or tabular data. Unlike many fusion methods, which often use simple concatenation or mixed decisions based on both modalities, including some advanced ones that limit themselves to specific transformations, our method stands out for its increased versatility and degrees of freedom, ensuring superior data utilization in our architectures. Remarkably, when benchmarked against state-of-the-art fusion techniques, our approach not only delivers superior results but also demonstrates their statistical significance.

In this study, we condition the processing of images on the patient's EHR, adopting an intuitive approach reminiscent of viewing the image through the lens of the patient's tabular data. An intriguing avenue for future research involves reversing this process: conditioning the EHR analysis on the image. Furthermore, beyond the realms of CNNs and MLPs, exploring the

integration of hypernetworks with other architectures opens up a promising pathway. Such adaptations could pave the way for robust data fusion techniques across a broader spectrum of data modalities.

In summary, this research not only identifies and tackles a crucial deep-learning challenge but also provides a robust solution through hypernetworks. The potential implications of this work extend from improving diagnostics to shaping the broader landscape of personalized medical care. As DNNs in the medical domain continue their rapid evolution, methods like ours, bridging the gap between diverse data modalities, are poised to play a significant role.

Acknowledgments

Funding: The paper was partially supported by the Ministry of Health (MoH 3-18509. T.R.R.) and the Israel Science Foundation (ISF 2497/19 T.R.R.) Partial funding was provided by the Natural Sciences and Engineering Research Council of Canada (RGPIN-2023-05152), the Canadian Institute for Advanced Research (CIFAR) Artificial Intelligence Chairs program, the Mila - Quebec AI Institute technology transfer program, Calcul Quebec, and the Digital Research Alliance of Canada (alliance.can.ca).

Datasets: Uk-Biobank - This research has been conducted using the UK Biobank Resource (www.ukbiobank.ac.uk).

CORR - Data were provided in part by the Consortium for Reliability and Reproducibility (http://fcon_1000.projects.nitrc.org/indi/CoRR/html/index.html)

ADNI - Data collection and sharing for this project was funded by the Alzheimer's Disease Neuroimaging Initiative (ADNI) (National Institutes of Health Grant U01 AG024904) and DOD ADNI (Department of Defense award number W81XWH-12-2-0012). ADNI is funded by the National Institute on Aging, the National Institute of Biomedical Imaging and Bioengineering, and through generous contributions from the following: AbbVie, Alzheimer's Association; Alzheimer's Drug Discovery Foundation; Araclon Biotech; BioClinica, Inc.; Biogen; Bristol-Myers Squibb Company; CereSpir, Inc.; Cogstate; Eisai Inc.; Elan Pharmaceuticals, Inc.; Eli Lilly and Company; EuroImmun; F. Hoffmann-La Roche Ltd and its affiliated company Genentech, Inc.; Fujirebio; GE Healthcare; IXICO Ltd.; Janssen Alzheimer Immunotherapy Research & Development, LLC.; Johnson & Johnson Pharmaceutical Research & Development LLC.; Lumosity; Lundbeck; Merck & Co., Inc.; Meso Scale Diagnostics, LLC.; NeuroRx Research; Neurotrack Technologies; Novartis Pharmaceuticals Corporation; Pfizer Inc.; Piramal Imaging; Servier; Takeda Pharmaceutical Company; and Transition Therapeutics. The Canadian Institutes of Health Research is providing funds to support ADNI clinical sites in Canada. Private sector contributions are facilitated by the Foundation for the National Institutes of Health (www.fnih.org). The grantee organization is the Northern California Institute for Research and Education, and the study is coordinated by the Alzheimer's Therapeutic Research Institute at the University of Southern California. ADNI data are disseminated by the Laboratory for Neuro Imaging at the University of Southern California.

GSP - Data were provided in part by the Brain Genomics Superstruct Project of Harvard University and the Massachusetts General Hospital, (Principal Investigators: Randy Buckner, Joshua Roffman, and Jordan Smoller), with support from the Center for Brain Science Neuroinformatics Research Group, the Athinoula A. Martinos Center for Biomedical Imaging, and the Center for Human Genetic Research. Twenty individual investigators at Harvard and MGH generously contributed data to GSP.

FCP - Data were provided in part by the Functional Connectomes Project (https://www.nitrc.org/projects/fcon_1000/).

ABIDE - Primary support for the work by Adriana Di Martino, and Michael P. Milham and his team was provided by the NIMH (K23MH087770), the Leon Levy Foundation, Joseph P. Healy and the Stavros Niarchos Foundation to the Child Mind Institute, NIMH award to MPM (R03MH096321), National Institute of Mental Health (NIMH5R21MH107045), Nathan S. Kline Institute of Psychiatric Research), Phyllis Green and Randolph Cowen to the Child Mind Institute.

PPMI - Data used in the preparation of this article were obtained from the Parkinson's Progression Markers Initiative (PPMI) database (www.ppmi-info.org/data). For up-to-date information on the study, visit www.ppmi-info.org. PPMI—a public-private partnership—is funded by the Michael J. Fox Foundation for Parkinson's Research and funding partners, including [list of the full names of all of the PPMI funding partners can be found at www.ppmi-info.org/fundingpartners].

ICBM - Data used in the preparation of this work were obtained from the International Consortium for Brain Mapping (ICBM) database (www.loni.usc.edu/ICBM). The ICBM project (Principal Investigator John Mazziotta, M.D., University of California, Los Angeles) is supported by the National Institute of Biomedical Imaging and BioEngineering. ICBM is the result of efforts of co-investigators from UCLA, Montreal Neurologic Institute, University of Texas at San Antonio, and the Institute of Medicine, Juelich/ Heinrich Heine University-Germany.

AIBL - Data used in the preparation of this article was obtained from the Australian Imaging Bio-markers and Lifestyle flagship study of aging (AIBL) funded by the Commonwealth Scientific and Industrial Research Organization (CSIRO) which was made available at the ADNI database (www.loni.usc.edu/ADNI). The AIBL researchers contributed data but did not participate in analysis or writing of this report. AIBL researchers are listed at www.aibl.csiro.au.

SLIM - Data were provided by the Southwest University Longitudinal Imaging Multimodal (SLIM) Brain Data Repository (http://fcon_1000.projects.nitrc.org/indi/retro/southwestuni_qiu_index.html).

IXI - Data were provided in part by the IXI database (<http://brain-development.org/>).

OASIS - OASIS is made available by Dr. Randy Buckner at the Howard Hughes Medical Institute (HHMI) at Harvard University, the Neuroinformatics Research Group (NRG) at Washington University School of Medicine, and the Biomedical Informatics Research Network (BIRN). Support for the

acquisition of this data and for data analysis was provided by NIH grants P50 AG05681, P01 AG03991, P20MH071616, RR14075, RR 16594, U24 RR21382, the Alzheimer's Association, the James S. McDonnell Foundation, the Mental Illness and Neuroscience Discovery Institute, and HHMI.

CNP - This work was supported by the Consortium for Neuropsychiatric Phenomics (NIH Roadmap for Medical Research grants UL1-DE019580, RL1MH083268, RL1MH083269, RL1DA024853, RL1MH083270, RL1LM009833, PL1MH083271, and PL1NS062410).

COBRE - Data were provided by the Center for Biomedical Research Excellence (COBRE) (http://fcon_1000.projects.nitrc.org/indi/retro/cobre.html).

CANDI - Data were provided in part by the Child and Adolescent Neuro Development Initiative - Schizophrenia Bulletin 2008 project.

Brainomics - Data were provided in part by the Brainomics project (<http://brainomics.cea.fr/>).

CamCAN - Data collection and sharing for this project was provided by the Cambridge Centre for Ageing and Neuroscience (CamCAN). CamCAN funding was provided by the UK Biotechnology and Biological Sciences Research Council (grant number BB/H008217/1), together with support from the UK Medical Research Council and University of Cambridge, UK.

References

- Aharon, S., Ben-Artzi, G., 2023. Hypernetwork-based adaptive image restoration, in: ICASSP 2023-2023 IEEE International Conference on Acoustics, Speech and Signal Processing (ICASSP), IEEE. pp. 1–5.
- Alexander, L.M., Escalera, J., Ai, L., Andreotti, C., Febre, K., Mangone, A., Vega-Potler, N., Langer, N., Alexander, A., Kovacs, M., et al., 2017. An open resource for transdiagnostic research in pediatric mental health and learning disorders. *Scientific data* 4, 1–26.
- Anderson, P., He, X., Buehler, C., Teney, D., Johnson, M., Gould, S., Zhang, L., 2018. Bottom-up and top-down attention for image captioning and visual question answering, in: Proceedings of the IEEE conference on computer vision and pattern recognition, pp. 6077–6086.
- Bäckström, K., Nazari, M., Gu, I.Y.H., Jakola, A.S., 2018. An efficient 3D deep convolutional network for Alzheimer's disease diagnosis using MR images, in: 2018 IEEE 15th International Symposium on Biomedical Imaging (ISBI 2018), pp. 149–153.
- Biswal, B.B., Mennes, M., Zuo, X.N., Gohel, S., Kelly, C., Smith, S.M., Beckmann, C.F., Adelstein, J.S., Buckner, R.L., Colcombe, S., et al., 2010. Toward discovery science of human brain function. *Proceedings of the national academy of sciences* 107, 4734–4739.
- Borisov, V., Leemann, T., Seßler, K., Haug, J., Pawelczyk, M., Kasneci, G., 2022. Deep neural networks and tabular data: a

- survey. *IEEE Transactions on Neural Networks and Learning Systems*.
- Buckner, R.L., Roffman, J.L., Smoller, J.W., 2014. Brain Genomics Superstruct Project (GSP).
- Carass, A., Roy, S., Jog, A., et al., 2017. Longitudinal multiple sclerosis lesion segmentation: resource and challenge. *NeuroImage* 148, 77–102.
- Chang, O., Flokas, L., Lipson, H., 2019. Principled weight initialization for hypernetworks, in: *International Conference on Learning Representations*.
- Chierigato, M., Frangiamore, F., Morassi, M., Baresi, C., Nici, S., Bassetti, C., Bnà, C., Galelli, M., 2022. A hybrid machine learning/deep learning COVID-19 severity predictive model from CT images and clinical data. *Scientific reports* 12, 4329.
- Coffey, C.E., Lucke, J.F., Saxton, J.A., Ratcliff, G., Unitas, L.J., Billig, B., Bryan, R.N., 1998. Sex differences in brain aging: a quantitative magnetic resonance imaging study. *Archives of neurology* 55, 169–179.
- Cole, J.H., Franke, K., 2017. Predicting age using neuroimaging: innovative brain ageing biomarkers. *Trends in neurosciences* 40, 681–690.
- Dawidowicz, G., Hirsch, E., Tal, A., 2023. LIMITR: Leveraging local information for medical image-text representation, in: *International Conference on computer Vision*.
- Di Martino, A., Yan, C.G., Li, Q., Denio, E., Castellanos, F.X., Alaerts, K., Anderson, J.S., Assaf, M., Bookheimer, S.Y., Dapretto, M., et al., 2014. The autism brain imaging data exchange: towards a large-scale evaluation of the intrinsic brain architecture in autism. *Molecular psychiatry* 19, 659–667.
- Dolci, G., Rahaman, M.A., Chen, J., Duan, K., Fu, Z., Abrol, A., Menegaz, G., Calhoun, V.D., 2022. A deep generative multimodal imaging genomics framework for alzheimer’s disease prediction, in: *2022 IEEE 22nd International Conference on Bioinformatics and Bioengineering (BIBE)*, pp. 41–44.
- El-Sappagh, S., Abuhmed, T., Riazul Islam, S., Kwak, K.S., 2020. Multimodal multitask deep learning model for Alzheimer’s disease progression detection based on time series data. *Neurocomputing* 412, 197–215.
- Ellis, K.A., Bush, A.I., Darby, D., De Fazio, D., Foster, J., Hudson, P., Lautenschlager, N.T., Lenzo, N., Martins, R.N., Maruff, P., et al., 2009. The australian imaging, biomarkers and lifestyle (aibl) study of aging: methodology and baseline characteristics of 1112 individuals recruited for a longitudinal study of alzheimer’s disease. *International psychogeriatrics* 21, 672–687.
- Esmailzadeh, S., Belivanis, D.I., Pohl, K.M., Adeli, E., 2018. End-to-end Alzheimer’s disease diagnosis and biomarker identification, in: Shi, Y., Suk, H.I., Liu, M. (Eds.), *Machine Learning in Medical Imaging*, Springer International Publishing, Cham. pp. 337–345.
- Feng, X., Lipton, Z.C., Yang, J., Small, S.A., Provenzano, F.A., Initiative, A.D.N., Initiative, F.L.D.N., et al., 2020. Estimating brain age based on a uniform healthy population with deep learning and structural magnetic resonance imaging. *Neurobiology of aging* 91, 15–25.
- Franke, K., Gaser, C., 2019. Ten years of BrainAGE as a neuroimaging biomarker of brain aging: what insights have we gained? *Frontiers in neurology*, 789.
- Fratiglioni, L., Grut, M., Forsell, Y., Viitanen, M., Grafström, M., Holmen, K., Ericsson, K., Bäckman, L., Ahlbom, A., Winblad, B., 1991. Prevalence of Alzheimer’s disease and other dementias in an elderly urban population. *Neurology* 41, 1886–1886.
- Frazier, J.A., Hodge, S.M., Breeze, J.L., Giuliano, A.J., Terry, J.E., Moore, C.M., Kennedy, D.N., Lopez-Larson, M.P., Caviness, V.S., Seidman, L.J., et al., 2008. Diagnostic and sex effects on limbic volumes in early-onset bipolar disorder and schizophrenia. *Schizophrenia bulletin* 34, 37–46.
- Glorot, X., Bengio, Y., 2010. Understanding the difficulty of training deep feedforward neural networks, in: *Proceedings of the thirteenth international conference on artificial intelligence and statistics, JMLR Workshop and Conference Proceedings*. pp. 249–256.
- Gorgolewski, K., Burns, C.D., Madison, C., Clark, D., Halchenko, Y.O., Waskom, M.L., Ghosh, S.S., 2011. Nipype: a flexible, lightweight and extensible neuroimaging data processing framework in python. *Frontiers in neuroinformatics* 5, 13.
- Ha, D., Dai, A.M., Quoc, V.L., 2016. Hypernetworks. *CoRR abs/1609.09106* (2016). arXiv preprint arXiv:1609.09106.
- Hager, P., Menten, M.J., Rueckert, D., 2023. Best of both worlds: Multimodal contrastive learning with tabular and imaging data, in: *Proceedings of the IEEE/CVF Conference on Computer Vision and Pattern Recognition (CVPR)*, pp. 23924–23935.
- He, K., Zhang, X., Ren, S., Sun, J., 2015a. Delving deep into rectifiers: Surpassing human-level performance on imagenet classification, in: *Proceedings of the IEEE international conference on computer vision*, pp. 1026–1034.
- He, K., Zhang, X., Ren, S., Sun, J., 2015b. Delving deep into rectifiers: Surpassing human-level performance on imagenet classification, in: *Proceedings of the IEEE international conference on computer vision*, pp. 1026–1034.
- He, K., Zhang, X., Ren, S., Sun, J., 2016. Identity mappings in deep residual networks, in: Leibe, B., Matas, J., Sebe, N., Welling, M. (Eds.), *Computer Vision – ECCV 2016*, Springer International Publishing, Cham. pp. 630–645.

- Heckemann, R.A., Hartkens, T., Leung, K.K., Zheng, Y., Hill, D.L., Hajnal, J.V., Rueckert, D., 2003. Information extraction from medical images: developing an e-science application based on the globus toolkit, in: Proceedings of the 2nd UK e-Science All Hands Meeting.
- Huang, S.C., Pareek, A., Seyyedi, S., Banerjee, I., Lungren, M.P., 2020. Fusion of medical imaging and electronic health records using deep learning: a systematic review and implementation guidelines. *NPJ digital medicine* 3, 136.
- Iglesias, J.E., Liu, C.Y., Thompson, P.M., Tu, Z., 2011. Robust brain extraction across datasets and comparison with publicly available methods. *IEEE Transactions on Medical Imaging* 30, 1617–1634.
- Jack Jr, C.R., Bernstein, M.A., Fox, N.C., Thompson, P., Alexander, G., Harvey, D., Borowski, B., Britson, P.J., L. Whitwell, J., Ward, C., et al., 2008. The alzheimer’s disease neuroimaging initiative (adni): Mri methods. *Journal of Magnetic Resonance Imaging: An Official Journal of the International Society for Magnetic Resonance in Medicine* 27, 685–691.
- Jenkinson, M., Beckmann, C.F., Behrens, T.E., Woolrich, M.W., Smith, S.M., 2012. Fsl. *NeuroImage* 62, 782–790. 20 YEARS OF fMRI.
- Lee, J., Burkett, B.J., Min, H.K., Senjem, M.L., Lundt, E.S., Botha, H., Graff-Radford, J., Barnard, L.R., Gunter, J.L., Schwarz, C.G., et al., 2022. Deep learning-based brain age prediction in normal aging and dementia. *Nature Aging* 2, 412–424.
- Letenneur, L., Gilleron, V., Commenges, D., Helmer, C., Orgozozo, J.M., Dartigues, J.F., 1999. Are sex and educational level independent predictors of dementia and alzheimer’s disease? incidence data from the paquid project. *Journal of Neurology, Neurosurgery & Psychiatry* 66, 177–183.
- Levakov, G., Rosenthal, G., Shelef, I., Riklin Raviv, T., Avidan, G., 2020. From a deep learning model back to the brain—identifying regional predictors and their relation to aging. *Human Brain Mapping* 41, 3235–3252.
- Littwin, G., Wolf, L., 2019. Deep meta functionals for shape representation, in: Proceedings of the IEEE/CVF International Conference on Computer Vision, pp. 1824–1833.
- Liu, M., Zhang, J., Adeli, E., Shen, D., 2018. Joint classification and regression via deep multi-task multi-channel learning for Alzheimer’s disease diagnosis. *IEEE Transactions on Biomedical Engineering* 66, 1195–1206.
- Liu, W., Wei, D., Chen, Q., Yang, W., Meng, J., Wu, G., Bi, T., Zhang, Q., Zuo, X.N., Qiu, J., 2017. Longitudinal test-retest neuroimaging data from healthy young adults in southwest china. *Scientific data* 4, 1–9.
- Marcus, D.S., Fotenos, A.F., Csernansky, J.G., Morris, J.C., Buckner, R.L., 2010. Open access series of imaging studies: longitudinal mri data in nondemented and demented older adults. *Journal of cognitive neuroscience* 22, 2677–2684.
- Marcus, D.S., Wang, T.H., Parker, J., Csernansky, J.G., Morris, J.C., Buckner, R.L., 2007. Open access series of imaging studies (oasis): cross-sectional mri data in young, middle aged, nondemented, and demented older adults. *Journal of cognitive neuroscience* 19, 1498–1507.
- Marek, K., Jennings, D., Lasch, S., Siderowf, A., Tanner, C., Simuni, T., Coffey, C., Kieburz, K., Flagg, E., Chowdhury, S., Poewe, W., Mollenhauer, B., Klinik, P.E., Sherer, T., Frasier, M., Meunier, C., Rudolph, A., Casaceli, C., Seibyl, J., Mendick, S., Schuff, N., Zhang, Y., Toga, A., Crawford, K., Ansbach, A., De Blasio, P., Piovella, M., Trojanowski, J., Shaw, L., Singleton, A., Hawkins, K., Eberling, J., Brooks, D., Russell, D., Leary, L., Factor, S., Sommerfeld, B., Hogarth, P., Pighetti, E., Williams, K., Standaert, D., Guthrie, S., Hauser, R., Delgado, H., Jankovic, J., Hunter, C., Stern, M., Tran, B., Leverenz, J., Baca, M., Frank, S., Thomas, C.A., Richard, I., Deeley, C., Rees, L., Sprenger, F., Lang, E., Shill, H., Obradov, S., Fernandez, H., Winters, A., Berg, D., Gauss, K., Galasko, D., Fontaine, D., Mari, Z., Gerstenhaber, M., Brooks, D., Malloy, S., Barone, P., Longo, K., Comery, T., Ravina, B., Grachev, I., Gallagher, K., Collins, M., Widnell, K.L., Ostrowizki, S., Fontoura, P., Ho, T., Luthman, J., van der Brug, M., Reith, A.D., Taylor, P., 2011. The parkinson progression marker initiative (ppmi). *Progress in Neurobiology* 95, 629–635. *Biological Markers for Neurodegenerative Diseases*.
- Mayer, A.R., Ruhl, D., Merideth, F., Ling, J., Hanlon, F.M., Bustillo, J., Canive, J., 2013. Functional imaging of the hemodynamic sensory gating response in schizophrenia. *Human brain mapping* 34, 2302–2312.
- Mazziotta, J.C., Toga, A.W., Evans, A., Fox, P., Lancaster, J., 1995. A probabilistic atlas of the human brain: Theory and rationale for its development: The international consortium for brain mapping (icbm). *NeuroImage* 2, 89–101.
- Menze, B.H., Jakab, A., Bauer, S., Kalpathy-Cramer, J., Farahani, K., Kirby, J., Burren, Y., Porz, N., Slotboom, J., Wiest, R., et al., 2014. The multimodal brain tumor image segmentation benchmark (brats). *IEEE transactions on medical imaging* 34, 1993–2024.
- Nooner, K.B., Colcombe, S.J., Tobe, R.H., Mennes, M., Benedict, M.M., Moreno, A.L., Panek, L.J., Brown, S., Zavitz, S.T., Li, Q., et al., 2012. The nki-rockland sample: a model for accelerating the pace of discovery science in psychiatry. *Frontiers in neuroscience* 6, 152.
- Pandeya, Y.R., Lee, J., 2021. Deep learning-based late fusion of multimodal information for emotion classification of music video. *Multimedia Tools and Applications* 80, 2887–2905.
- Peng, H., Gong, W., Beckmann, C.F., Vedaldi, A., Smith, S.M., 2021. Accurate brain age prediction with lightweight deep neural networks. *Medical Image Analysis* 68, 101871.

- Perez, E., Strub, F., de Vries, H., Dumoulin, V., Courville, A., 2018. FiLM: visual reasoning with a general conditioning layer. *Proceedings of the AAAI Conference on Artificial Intelligence* 32.
- Piçarra, C., Glocker, B., 2023. Analysing race and sex bias in brain age prediction, in: *Workshop on Clinical Image-Based Procedures*, Springer. pp. 194–204.
- Pinel, P., Fauchereau, F., Moreno, A., Barbot, A., Lathrop, M., Zelenika, D., Le Bihan, D., Poline, J.B., Bourgeron, T., Dehaene, S., 2012. Genetic variants of *foxp2* and *kiaa0319/ttrap/them2* locus are associated with altered brain activation in distinct language-related regions. *Journal of Neuroscience* 32, 817–825.
- Poldrack, R.A., Congdon, E., Triplett, W., Gorgolewski, K., Karlsgodt, K., Mumford, J., Sabb, F., Freimer, N., London, E., Cannon, T., et al., 2016. A phenome-wide examination of neural and cognitive function. *Scientific data* 3, 1–12.
- Prabhu, S.S., Berkebile, J.A., Rajagopalan, N., Yao, R., Shi, W., Giuste, F., Zhong, Y., Sun, J., Wang, M.D., 2022. Multimodal deep learning models for Alzheimer’s disease prediction using MRI and EHR, in: *2022 IEEE 22nd International Conference on Bioinformatics and Bioengineering (BIBE)*, IEEE. pp. 168–173.
- Qiu, S., Chang, G.H., Panagia, M., Gopal, D.M., Au, R., Kollachalama, V.B., 2018. Fusion of deep learning models of MRI scans, mini-mental state examination, and logical memory test enhances diagnosis of mild cognitive impairment. *Alzheimer’s and Dementia: Diagnosis, Assessment and Disease Monitoring* 10, 737–749.
- Radford, A., Kim, J.W., Hallacy, C., Ramesh, A., Goh, G., Agarwal, S., Sastry, G., Askell, A., Mishkin, P., Clark, J., et al., 2021. Learning transferable visual models from natural language supervision, in: *International conference on machine learning*, PMLR. pp. 8748–8763.
- Rao, Y., Ganaraja, B., Murlimanju, B., Joy, T., Krishnamurthy, A., Agrawal, A., 2022. Hippocampus and its involvement in Alzheimer’s disease: a review. *3 Biotech* 12.
- Reinhold, J.C., Dewey, B.E., Carass, A., Prince, J.L., 2018. Evaluating the impact of intensity normalization on mr image synthesis. *CoRR abs/1812.04652*. [arXiv:1812.04652](https://arxiv.org/abs/1812.04652).
- Salta, E., Lazarov, O., Fitzsimons, P., Tanzi, R., Lucassen, P., Choi, S., 2023. Adult hippocampal neurogenesis in Alzheimer’s disease: A roadmap to clinical relevance. *Cell Stem Cell* 30, 120–136.
- Shafto, M.A., Tyler, L.K., Dixon, M., Taylor, J.R., Rowe, J.B., Cusack, R., Calder, A.J., Marslen-Wilson, W.D., Duncan, J., Dalgleish, T., et al., 2014. The cambridge centre for ageing and neuroscience (cam-can) study protocol: a cross-sectional, lifespan, multidisciplinary examination of healthy cognitive ageing. *BMC neurology* 14, 1–25.
- Simonyan, K., Zisserman, A., 2014. Very deep convolutional networks for large-scale image recognition. *arXiv preprint arXiv:1409.1556*.
- Spasov, S.E., Passamonti, L., Duggento, A., Liò, P., Toschi, N., 2018. A multi-modal convolutional neural network framework for the prediction of Alzheimer’s disease, in: *2018 40th Annual International Conference of the IEEE Engineering in Medicine and Biology Society (EMBC)*, pp. 1271–1274.
- Sudlow, C., Gallacher, J., Allen, N., Beral, V., Burton, P., Danesh, J., Downey, P., Elliott, P., Green, J., Landray, M., et al., 2015. Uk biobank: an open access resource for identifying the causes of a wide range of complex diseases of middle and old age. *PLoS medicine* 12, e1001779.
- Sui, J., Zhi, D., Calhoun, V.D., 2023. Data-driven multimodal fusion: approaches and applications in psychiatric research. *Psychoradiology*, kkad026.
- Tustison, N.J., Avants, B.B., Cook, P.A., Zheng, Y., Egan, A., Yushkevich, P.A., Gee, J.C., 2010. N4itk: Improved n3 bias correction. *IEEE Transactions on Medical Imaging* 29, 1310–1320.
- Venugopalan, J., Tong, L., Hassanzadeh, H.R., Wang, M.D., 2021. Multimodal deep learning models for early detection of Alzheimer’s disease stage. *Scientific reports* 11, 3254.
- Vinyals, O., Toshev, A., Bengio, S., Erhan, D., 2015. Show and tell: A neural image caption generator, in: *Proceedings of the IEEE conference on computer vision and pattern recognition*, pp. 3156–3164.
- Wang, L., Li, Y., Lazebnik, S., 2016. Learning deep structure-preserving image-text embeddings, in: *Proceedings of the IEEE Conference on Computer Vision and Pattern Recognition (CVPR)*.
- Wang, S.H., Phillips, P., Sui, Y., Liu, B., Yang, M., Cheng, H., 2018. Classification of Alzheimer’s disease based on eight-layer convolutional neural network with leaky rectified linear unit and max pooling. *Journal of medical systems* 42, 1–11.
- Wang, Z., Wu, Z., Agarwal, D., Sun, J., 2022. Medclip: Contrastive learning from unpaired medical images and text. *arXiv preprint arXiv:2210.10163*.
- Wen, J., Thibaud-Sutre, E., Diaz-Melo, M., Samper-González, J., Routier, A., Bottani, S., Dormont, D., Durrleman, S., Burgos, N., Colliot, O., et al., 2020. Convolutional neural networks for classification of Alzheimer’s disease: Overview and reproducible evaluation. *Medical image analysis* 63, 101694.
- Wolf, T.N., Pölsterl, S., Wachinger, C., 2022. DAFT: A universal module to interweave tabular data and 3D images in CNNs. *NeuroImage* 260, 119505.
- Wydmański, W., Bulenok, O., Śmieja, M., 2023. HyperTab: Hypernetwork approach for deep learning on small tabular datasets. *arXiv preprint arXiv:2304.03543*.

Xu, K., Ba, J., Kiros, R., Cho, K., Courville, A., Salakhudinov, R., Zemel, R., Bengio, Y., 2015. Show, attend and tell: Neural image caption generation with visual attention, in: International conference on machine learning, PMLR. pp. 2048–2057.

Yang, H., Zhou, T., Zhou, Y., Zhang, Y., Fu, H., 2023. Flexible fusion network for multi-modal brain tumor segmentation. *IEEE Journal of Biomedical and Health Informatics* 27, 3349–3359.

Zhang, C., Zhang, C., Zhang, M., Kweon, I.S., 2023. Text-to-image diffusion model in generative ai: A survey. *arXiv preprint arXiv:2303.07909*.

Zhang, H., Xu, T., Li, H., Zhang, S., Wang, X., Huang, X., Metaxas, D.N., 2018. Stackgan++: Realistic image synthesis with stacked generative adversarial networks. *IEEE transactions on pattern analysis and machine intelligence* 41, 1947–1962.

Zhou, T., Thung, K.H., Zhu, X., Shen, D., 2019. Effective feature learning and fusion of multimodality data using stage-wise deep neural network for dementia diagnosis. *Human brain mapping* 40, 1001–1016.

Zuo, X.N., Anderson, J.S., Bellec, P., Birn, R.M., Biswal, B.B., Blautzik, J., Breitner, J., Buckner, R.L., Calhoun, V.D., Castellanos, F.X., et al., 2014. An open science resource for establishing reliability and reproducibility in functional connectomics. *Scientific data* 1, 1–13.

Appendix

Appendix A. Brain Age Prediction Data

Table A.3 presents the datasets used for the brain age prediction task. The preprocessing pipeline of the T1-weighted MRI scans is identical to the one proposed in (Levakov et al., 2020), using Nipype (Gorgolewski et al., 2011). Initially, RobustFov Jenkinson et al. (2012) was employed to remove the neck and shoulders from each scan. Subsequently, Robex Iglesias et al. (2011) was utilized for brain extraction, followed by expanding the brain mask to encompass the CSF surrounding the brain. The correction for intensity non-uniformity was carried out using N4BiasFieldCorrection Tustison et al. (2010). Further, intensity normalization was implemented using fuzzy c-means and WM-based mean normalization Reinhold et al. (2018). Ultimately, the images were resampled to a resolution of 1.75 mm³ and cropped to a 90x120x99 voxels box centered around the brain mask’s center of mass.

Appendix B. AD data splitting, model training and evaluation

Figure B.7 visualize the data partitioning and well as the evaluation method for the cross validation experiments of the AD classification.

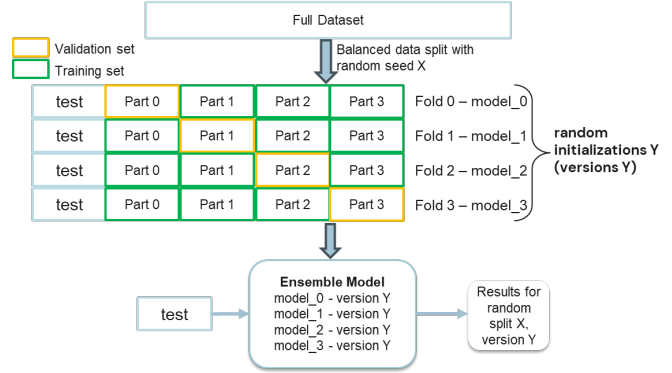


Figure B.7: Data Splitting and model training and evaluation illustration for AD Classification Task: each version is a different random initialization of a model. The entire process is performed using three random seeds with three versions for each, i.e., nine cross-validation experiments all together.

Appendix C. AD Classification Confusion Matrices

Figure C.8 presents the confusion matrices for our hyperfusion and the compared methods for the AD classification task, providing more insight on the relative classification abilities for each subgroup.

Appendix D. Ablation Study: Class Weights for the AD Classification Task

As mentioned in the main manuscript, we trained the networks with weighted categorical cross entropy loss. The weights of the classes influence the relative scores between the different classes. The late fusion method (Prabhu et al., 2022) obtained higher PRC scores at the expense of weaker BAC results due to the inherent trade-off between these two metrics using imbalanced datasets. We note that for other combinations of class weights our HyperFusion method achieved higher scores in all the reported metrics. Table D.4 presents the results obtained by our method, trained with different class weight configurations as well as the reported results of the late fusion method to support our claim.

Table D.4: AD classification results for the proposed HyperFusion and the late-fusion method. The first row presents the scores obtained our model that trained using different class weight configurations in the weighted cross entropy loss function. The second row presents reported results of the late-fusion method of (Prabhu et al., 2022). The comparison is based on three metrics detailed in main manuscript.

model	BA	PRC	f1 macro
HyperFusion - different class weights	0.6539	0.6563	0.6433
Reported late-fusion results (Prabhu et al., 2022)	0.6330	0.6473	0.6240

Table A.3: List of all datasets used for the brain age prediction task. For each dataset, the number of available subjects (N), the sex distribution, and the mean and std of the age distribution are provided.

Study/database	N	Age - mean (\pm std)	Sex (M:F)
UK Biobank (Sudlow et al., 2015)	17,088	63.1 (\pm 7.5)	8,118:8,970
Consortium for Reliability and Reproducibility, CoRR (Zuo et al., 2014)	1,350	26.1 (\pm 15.9)	661:689
Alzheimer's Disease Neuroimaging Initiative, ADNI (Jack Jr et al., 2008)	659	72.9 (\pm 6.0)	432:227
Brain Genomics Superstruct Project, GSP (Buckner et al., 2014)	1,099	21.5 (\pm 2.9)	469:630
Functional Connectomes Project, FCP (Biswal et al., 2010)	922	28.2 (\pm 13.9)	393:529
Autism Brain Imaging Data Exchange, ABIDE (Di Martino et al., 2014)	506	16.9 (\pm 7.7)	411:95
Parkinson's Progression Markers Initiative, PPMI (Marek et al., 2011)	172	60.3 (\pm 11.0)	105:67
International Consortium for Brain Mapping, ICBM (Mazziotta et al., 1995)	592	30.9 (\pm 12.5)	319:273
Australian Imaging, Biomarkers and Lifestyle, AIBL (Ellis et al., 2009)	604	73.0 (\pm 6.6)	268:335
Southwest University LongitudinalImaging Multimodal, SLIM (Liu et al., 2017)	571	20.1 (\pm 1.3)	251:320
Information extraction from Images, IXI (Heckemann et al., 2003)	562	48.2 (\pm 16.5)	251:311
Open Access Series of Imaging Studies, OASIS (Marcus et al., 2007, 2010)	401	51.7 (\pm 24.9)	144:257
Consortium for Neuropsychiatric Phenomics, CNP (Poldrack et al., 2016)	124	31.5 (\pm 8.8)	65:59
Center for Biomedical Research Excellence, COBRE (Mayer et al., 2013)	74	35.8 (\pm 11.6)	51:23
Child and Adolescent NeuroDevelopment Initiative, CANDI (Frazier et al., 2008)	29	10.0 (\pm 2.9)	17:12
Brainomics (Pinel et al., 2012)	68	25.4 (\pm 7.1)	31:37
Cambridge Centre for Ageing and Neuroscience, CamCAN (Shafto et al., 2014)	652	54.3 (\pm 18.6)	322:330
Child Mind Institute - Healthy Brain Network, HBN (Alexander et al., 2017)	304	10.0 (\pm 3.7)	164:140
Nathan Kline Institute-Rockland Sample, NKI (Nooner et al., 2012)	914	37.1 (\pm 21.7)	359:555
Overall	26,691	53.7 (\pm 19.5)	12,831:13,859

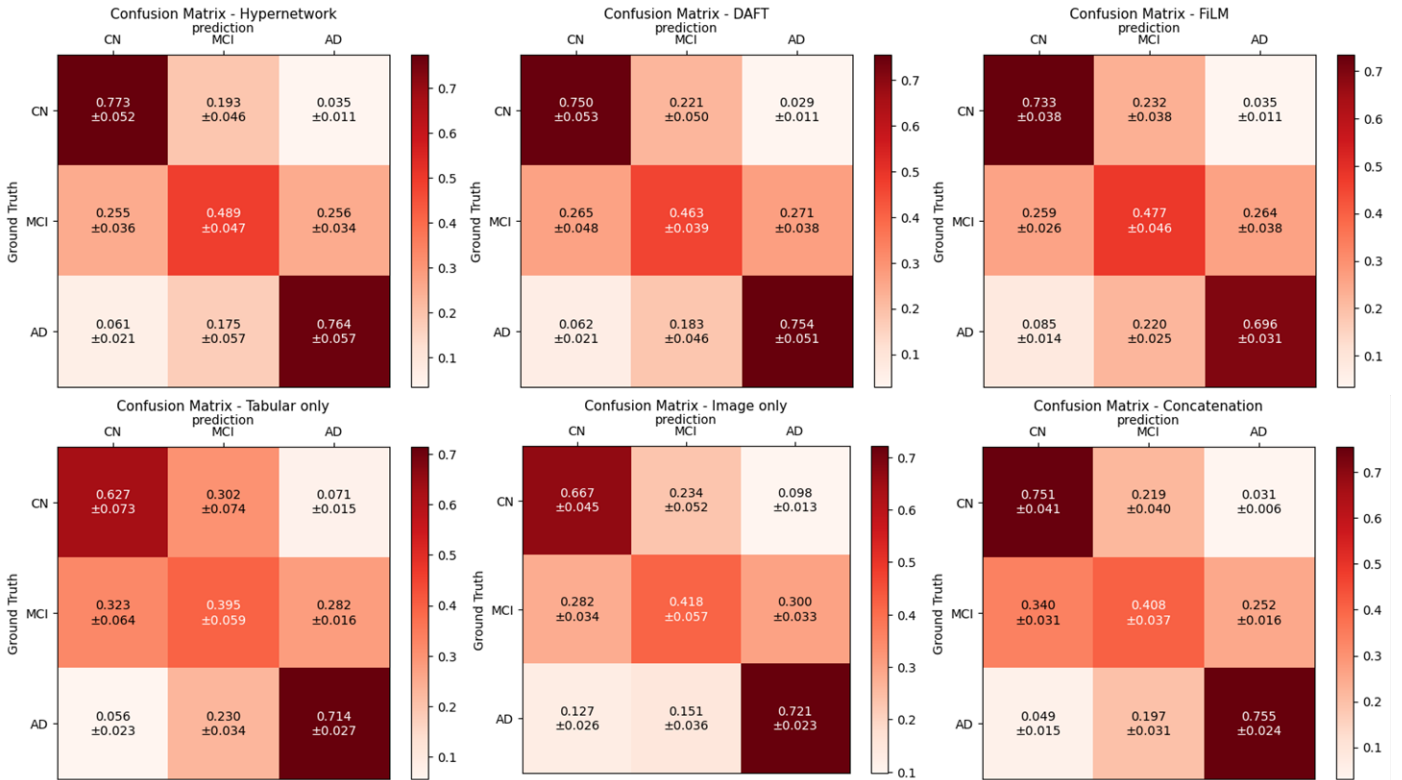


Figure C.8: Confusion matrices for the AD classification task. Each matrix represents the predicted results versus the ground truth, with row-normalization for easier interpretation. Each cell in a matrix contains the mean and standard deviation values calculated over all conducted experiments.